^{55}Mn ESE−ENDOR of a Mixed Valence Mn(III)Mn(IV) Complex: Comparison with the Mn Cluster of the Photosynthetic Oxygen-Evolving Complex

David W. Randall,[†] Bradley E. Sturgeon,[†] James A. Ball,[†] Gary A. Lorigan,[†] Michael K. Chan,[‡] Melvin P. Klein,[§] William H. Armstrong,[⊥] and R. David Britt*,[†]

Contribution from the Department of Chemistry, University of California, Davis, California 95616, Structural Biology Division, Lawrence Berkeley Laboratory, University of California, Berkeley, California 94720, and Department of Chemistry, Eugene F. Merkert Chemistry Center, Boston College, Chestnut Hill, Massachusetts 02167-3860

Received August 7, 1995[⊗]

Abstract: Analysis of ^{55}Mn electron spin echo−electron nuclear double resonance (ESE−ENDOR) spectra obtained on a dinuclear mixed valence Mn(III)Mn(IV) complex [di-μ-oxotetrakis(2,2′-bipyridine)dimanganese(III,IV)] (**1**) reveals the hyperfine and nuclear quadrupolar parameters for the spin $I = 5/2$ ^{55}Mn nucleus of both Mn(III) and Mn(IV) ions. The following parameters are obtained: for Mn(IV), $A_\perp = +212$ MHz, $A_\parallel = +231$ MHz, $P_\parallel = 3e^2Qq/40 = +2.0$ MHz, and $\eta = 0.3$, and for Mn(III), $A_\perp = -480$ MHz, $A_\parallel = -360$ MHz, $P_\parallel = -4.5$ MHz, and $\eta = 0.1$. The ^{55}Mn ESE−ENDOR data obtained on the $g = 2$ Mn multiline EPR signal of the S_2 state of the photosystem II oxygen-evolving complex demonstrate that this EPR signal cannot arise from a dinuclear Mn(III)-Mn(IV) center. The ENDOR spectra are consistent with a tetranuclear Mn cluster origin for the photosystem II multiline EPR signal.

Introduction

Manganese clusters are utilized in a number of metalloenzymes. As recently inventoried by Dismukes,[1] many of these enzymes employ dinuclear Mn clusters at their active sites.[2−6] An intensively studied example of such a dinuclear Mn enzyme is manganese catalase, which catalyzes hydrogen peroxide disproportionation.[6−13] The photosystem II (PS II) oxygen-evolving complex (OEC) utilizes four Mn ions in the photosynthetic water-splitting chemistry. The OEC poised in the S_2 state of the oxygen-evolving cycle[14] presents Mn EPR signals at either $g = 2$[15] or $g = 4.1$[16,17] depending on the specifics of sample illumination or treatment. On the basis of details of spin state interconversions between $g = 2$ and $g = 4.1$ Mn signal forms[18,19] and EPR simulations of the $g = 2$ "multiline" EPR signal,[20−24] the current predominant model places the four Mn ions in a single magnetically-coupled tetranuclear cluster. However, on the basis of successful multifrequency EPR simulations of the $g = 2$ multiline signal using a dinuclear Mn cluster model with large ^{55}Mn nuclear quadrupole interactions and large anisotropic hyperfine couplings, Åhrling and Pace proposed that such a dinuclear Mn cluster exists magnetically isolated within the OEC.[25]

Details of the electronic structure of a paramagnetic center such as a mixed valence Mn cluster can be provided by EPR spectroscopy and EPR-derived techniques such as electron nuclear double resonance (ENDOR) and electron spin echo envelope modulation (ESEEM).[26−29] For biological complexes of unknown structure it is often useful to compare results

[†] University of California, Davis.
[‡] Present address: Department of Chemistry and Department of Biochemistry, Ohio State University, Columbus, OH 43210.
[§] University of California, Berkeley.
[⊥] Boston College.
[⊗] Abstract published in *Advance ACS Abstracts*, November 1, 1995.

(1) Dismukes, G. C. In *Bioinorganic Catalysis*; Reekijk, J., Ed.; Marcel Dekker: New York, 1993; pp 317−346.
(2) Reczkowsi, R. S.; Ash, D. E. *J. Am. Chem. Soc.* **1992**, *114*, 10992−10994.
(3) Collyer, C. A.; Henrick, K.; Blow, D. M. *J. Mol. Biol.* **1990**, *212*, 211−235.
(4) Willing, A.; Follmann, H.; Auling, G. *Eur. J. Biochem.* **1988**, *170*, 603−611.
(5) Davies, J. F., II; Hostomska, Z.; Hostomsky, Z.; Jordan, S. R.; Matthews, D. A. *Science* **1991**, *252*, 88−95.
(6) Penner-Hahn, J. E. In *Manganese Enzymes*; Pecoraro, V. L., Ed.; VCH Publishers: New York, 1992; pp 29−45.
(7) Fronko, R. M.; Penner-Hahn, J. E.; Bender, C. J. *J. Am. Chem. Soc.* **1988**, *110*, 7554−7555.
(8) Dikanov, S. A.; Tsvetkov, Y. D.; Khangulov, S. V.; Gol'dfel'd, M. G. *Dokl. Biophys.* **1989**, *302*, 174−177.
(9) Khangulov, S. V.; Voyevodskaya, N. V.; Varynin, V. V.; Grebenko, A. I.; Melik-Adamyan, V. R. *Biophysics* **1987**, *32*, 1044−1051.
(10) Khangulov, S.; Sivaraja, M.; Barynin, V. V.; Dismukes, G. C. *Biochemistry* **1993**, *32*, 4912−4924.
(11) Khangulov, S. V.; Pessiki, P. J.; Barynin, V. V.; Ash, D. E.; Dismukes, G. C. *Biochemistry* **1995**, *34*, 2015−2025.
(12) Haddy, A.; Waldo, G. S.; Sands, R. H.; Penner-Hahn, J. E. *Inorg. Chem.* **1994**, *33*, 2677−2682.
(13) Zheng, M.; Khangulov, S. V.; Dismukes, G. C.; Barynin, V. V. *Inorg. Chem.* **1994**, *33*, 382−387.
(14) Kok, B.; Forbush, B.; McGloin, M. *Photochem. Photobiol.* **1970**, *11*, 457−475.
(15) Dismukes, G. C.; Siderer, Y. *Proc. Natl. Acad. Sci. U.S.A.* **1981**, *78*, 247−278.
(16) Casey, J. L.; Sauer, K. *Biochim. Biophys. Acta* **1984**, *767*, 21−28.
(17) Zimmermann, J.-L.; Rutherford, A. W. *Biochim. Biophys. Acta* **1984**, *767*, 160−167.
(18) Kim, D. H.; Britt, R. D.; Klein, M. P.; Sauer, K. *J. Am. Chem. Soc.* **1990**, *112*, 9389−9391.
(19) Brudvig, G. W. In *Advanced EPR: Applications in Biology and Biochemistry*; Hoff, A. J., Ed.; Elsevier: Amsterdam, 1989; pp 839−863.
(20) Kusunoki, M. *Chem. Phys. Lett.* **1992**, *197*, 108−116.
(21) Zheng, M.; Dismukes, G. C. In *Research in Photosynthesis*; Murata, N., Ed.; Kluwer Academic Publishers: Dordrecht, The Netherlands, 1992; pp 305−308.
(22) Zheng, M.; Dismukes, G. C. *Inorg. Chem.*, in press.
(23) Bonvoisin, J.; Blondin, G.; Girerd, J.-J.; Zimmermann, J.-L. *Biophys. J.* **1992**, *61*, 1076−1086.
(24) Belinskii, M. I. *Chem. Phys.* **1994**, *179*, 1−22.
(25) Åhrling, K. A.; Pace, R. J. *Biophys. J.* **1995**, *68*, 2081−2090.
(26) Britt, R. D. *Curr. Opin. Struct. Biol.* **1993**, *3*, 774−779.
(27) Hoffman, B. M.; DeRose, V. J.; Doan, P. E.; Gurbiel, R. J.; Houseman, A. L. P.; Telser, J. In *Biological Magnetic Resonance*; Berliner, L. J., Reuben, J., Eds.; Plenum Press: New York, 1993; pp 151−218.
(28) Thomann, H.; Bernardo, M. In *Methods in Enzymology*; Riordan, J. F., Vallee, B. L., Eds.; Academic Press: San Diego, 1993; pp 118−189.

0002-7863/95/1517-11780$09.00/0

obtained with such spectroscopies to those obtained on "model" compounds of well-characterized structure.[30,31] The work described in this paper takes this approach. We have performed ENDOR experiments on the 100% natural abundance spin $I = 5/2$ ^{55}Mn nuclei of a dinuclear Mn(III)Mn(IV) exchange-coupled compound (di-μ-oxotetrakis(2,2′-bipyridine)dimanganese-(III,IV) perchlorate (**1**)) with a well-defined crystal structure[32] and extensively studied magnetic properties.[13,33,34] The ^{55}Mn ENDOR results of this model compound are compared with those obtained on the Mn cluster of the OEC poised in the S_2 state form giving rise to the $g = 2$ multiline EPR signal.

We are interested in obtaining these ^{55}Mn ENDOR results because the high spectral density of EPR transitions in multinuclear Mn clusters combined with the effects of inhomogeneous broadening leads to EPR spectra with limited resolution. For the general case of an electron spin $S = 1/2$ system coupled to k different classes of n_i equivalent spin I_i nuclei, the number of allowed EPR transitions is given by the well-known expression

$$\text{number of EPR transitions} = \prod_{i=1}^{k}(2n_iI_i + 1) \qquad (1)$$

The number of EPR transitions increases geometrically with the number of classes of coupled nuclei. For example, an $S = 1/2$ state of a tetranuclear Mn complex with inequivalent isotropic hyperfine interactions would present 1296 transitions in the EPR spectrum. However, only approximately 19 lines are resolved in the $g = 2$ multiline EPR spectrum of the OEC, most often modeled as arising from a tetranuclear Mn cluster. The EPR absorption spectrum is actually dominated by a broad, near Gaussian line shape that results from the dense spectral overlap of these transitions.[35,36] The spectral overlap is even more severe with the $g = 4.1$ signal arising from the cluster, which is devoid of ^{55}Mn hyperfine structure except for the special case of oriented, ammonia-treated membranes.[18,37] Even dinuclear Mn(III)Mn(IV) model compounds show limited resolution, as only 16 hyperfine lines are clearly resolved in the EPR spectra that result from the overlapping powder patterns of 36 separate EPR transitions.[30,33,38-44] Such loss of resolution can make extracting the spin Hamiltonian parameters from the EPR spectrum alone difficult.

In contrast to the situation with the EPR spectrum, the number of nuclear spin transitions observed in an ENDOR experiment increases only additively with the number of inequivalent classes of coupled nuclei. Therefore, the number of ENDOR transitions should remain manageable for small Mn clusters such as that of the photosynthetic OEC. Moreover, ENDOR provides sensitivity superior to EPR in elucidating nuclear quadrupolar interactions for $I \geq 1$ nuclei such as ^{55}Mn since the nuclear quadrupole interaction affects the ENDOR spectrum to first order. In contrast, the nuclear quadrupole interaction affects the EPR spectrum only to second and higher orders, and its small effects can therefore easily be masked by a plethora of inhomogeneous broadening effects such as strain in more dominant parameters and/or unresolved superhyperfine interactions.

Magnetic Resonance Background and Theory

Complex **1** is strongly antiferromagnetically exchange coupled ($J = -150$ cm^{-1}), resulting in an $S = 1/2$ ground state which is almost exclusively occupied at the experimental temperature of 4.2 K.[33] In analyzing the spin Hamiltonian of this system, it is convenient to convert from an uncoupled basis set where the electronic spin projections (m_{S_i}) of the individual ions commute with the spin Hamiltonian (an $|S_1, S_2, m_{S_1}, m_{S_2}\rangle$ basis set) to a coupled basis in which the vector sum of S_1 and S_2, $S_T = \vec{S}_1 + \vec{S}_2$, and the coupled electronic spin projection, $-|\vec{S}_1 + \vec{S}_2| \leq m_{S_T} \leq +|\vec{S}_1 + \vec{S}_2|$, commute with the spin Hamiltonian (an $|S_T, m_{S_T}, S_1, S_2\rangle$ basis set).[13,33,45] In the uncoupled representation the spin Hamiltonian is

$$\mathcal{H} = -2J\vec{S}_1\cdot\vec{S}_2 + \sum_{i=1}^{2}[\beta'\vec{B}\cdot\mathbf{g}_i\cdot\vec{S}_i + \vec{S}_i\cdot\mathbf{D}_i\cdot\vec{S}_i + \vec{S}_i\cdot\mathbf{a}_i\cdot\vec{I}_i - g_N\beta'_N\vec{B}\cdot\vec{I}_i + \vec{I}_i\cdot\mathbf{P}_i\cdot\vec{I}_i] \quad (2)$$

where J is the isotropic exchange interaction, the sum is over the two Mn ions, β' is the Bohr magneton in units of MHz/G, $\vec{B}$ is the magnetic field vector, the **g** matrix describes the interaction between $\vec{B}$ and the electron spin operator $\vec{S}_i$, $\vec{I}_i$ is the nuclear spin operator, $\mathbf{a}_i$, $\mathbf{D}_i$, and $\mathbf{P}_i$ are the intrinsic (isolated ion) hyperfine, zero field splitting, and nuclear quadrupole interaction matrices for Mn ion i, g_N is the nuclear g value of ^{55}Mn, and β'_N is the nuclear magneton in MHz/G. In the coupled representation the spin Hamiltonian for the $S_T = 1/2$ ground state takes on a simpler form:[13,33,45,46]

$$\mathcal{H} = \beta'\vec{B}\cdot\mathbf{g}\cdot\vec{S}_T + \sum_{i=1}^{2}[\vec{S}_T\cdot\mathbf{A}_i\cdot\vec{I}_i - g_N\beta'_N\vec{B}\cdot\vec{I}_i + \vec{I}_i\cdot\mathbf{P}_i\cdot\vec{I}_i] \quad (3)$$

where the sum is over the two Mn nuclei. Here $\mathbf{A}_i$ represents the effective hyperfine interaction matrix (*vide infra*). Since $S_T = 1/2$, no **D** terms enter the coupled representation Hamiltonian for the ground spin state. A consequence of switching to the coupled basis set is that terms in the uncoupled spin Hamiltonian involving $\vec{S}_i$ are scaled by a projection operator in the coupled spin Hamiltonian: $\vec{S}_i\cdot\vec{S}_T/S_T^2$, where $i = 1$ and 2.

(29) Dikanov, S. A.; Tsvetkov, Y. D. *Electron spin echo envelope modulation (ESEEM) spectroscopy*; CRC Press: Boca Raton, FL, 1992.
(30) Wieghardt, K. *Angew. Chem., Int. Ed. Engl.* **1989**, *28*, 1153-1172.
(31) Armstrong, W. H. In *Manganese Redox Enzymes*; Pecoraro, V. L., Ed.; VCH Publishers: New York, 1992; pp 261-286.
(32) Plaksin, P. M.; Stoufer, R. C.; Mathew, M.; Palenik, G. J. *J. Am. Chem. Soc.* **1972**, *94*, 2121-2122.
(33) Cooper, S. R.; Dismukes, G. C.; Klein, M. P.; Calvin, M. *J. Am. Chem. Soc.* **1978**, *100*, 7248-7252.
(34) Gamelin, D. R.; Kirk, M. L.; Stemmler, T. L.; Pal, S.; Armstrong, W. H.; Penner-Hahn, J. E.; Solomon, E. I. *J. Am. Chem. Soc.* **1994**, *116*, 2392-2399.
(35) Britt, R. D.; Zimmermann, J.-L.; Sauer, K.; Klein, M. P. *J. Am. Chem. Soc.* **1989**, *111*, 3522-3532.
(36) Britt, R. D.; Lorigan, G. A.; Sauer, K.; Klein, M. P.; Zimmermann, J.-L. *Biochim. Biophys. Acta* **1992**, *1040*, 95-101.
(37) Kim, D. H.; Britt, R. D.; Klein, M. P.; Sauer, K. *Biochemistry* **1992**, *31*, 541-547.
(38) Sheats, J. E.; Czernuszewicz, R. S.; Dismukes, G. C.; Rheingold, A. L.; Petrouleas, V.; Stubbe, J.; Armstrong, W. H.; Beer, R. H.; Lippard, S. J. *J. Am. Chem. Soc.* **1987**, *109*, 1435-1444.
(39) Suzuki, M.; Tokura, S.; Suhara, M.; Uehara, A. *Chem. Lett.* **1988**, 477-480.
(40) Hagen, K. S.; Armstrong, W. H.; Hope, H. *Inorg. Chem.* **1988**, *27*, 967-9.
(41) Brewer, K. J.; Calvin, M.; Lumpkin, R. S.; Otvos, J. W.; Spreer, L. O. *Inorg. Chem.* **1989**, *28*, 4446-4451.
(42) Goodson, P. A.; Hodgson, D., J.; Glerup, J.; Michelsen, K.; Weihe, H. *Inorg. Chim. Acta* **1992**, *197*, 141-147.
(43) Pessiki, P. J.; Khangulov, S. V.; Ho, D. M.; Dismukes, G. C. *J. Am. Chem. Soc.* **1994**, *116*, 891-897.
(44) These 16-line spectra that bear some resemblance to the $g = 2$ multiline EPR spectrum of the OEC arise from valence-trapped Mn(III)-Mn(IV) clusters. A hypothetical valence-delocalized cluster with equivalent Mn sites would give rise to an 11-line spectrum (eq 1) with no resemblence to the OEC spectrum.
(45) Bencini, A.; Gatteschi, D. *Electron Paramagnetic Resonance of Exchange Coupled Systems*; Springer-Verlag: Berlin, 1989; pp 48-66.
(46) Tan, X.-L.; Gultneh, Y.; Sarneski, J. E.; Scholes, C. P. *J. Am. Chem. Soc.* **1991**, *113*, 7853-7858.

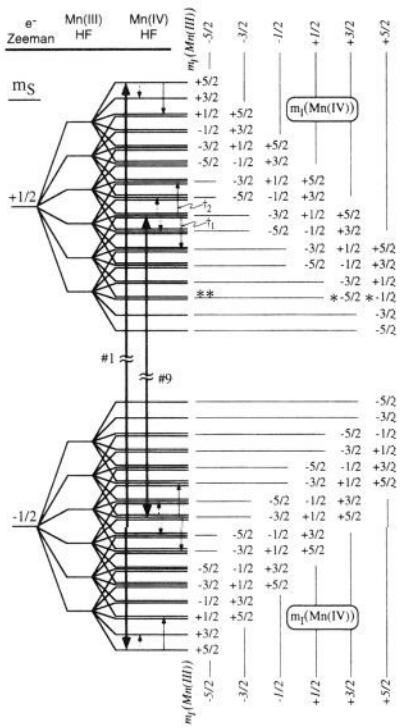

Figure 1. Energy level splitting diagram for an isotropic $S = 1/2$, $I_{Mn(III)} = 5/2$, $I_{Mn(IV)} = 5/2$ spin system where $\beta'\vec{B}\cdot\mathbf{g}\cdot\vec{S}_T$ dominates the spin Hamiltonian and $-\mathbf{A}_{Mn(III)} = +2\mathbf{A}_{Mn(IV)}$. The labeling of m_I levels is based on a negative intrinsic (isolated ion) hyperfine interaction for both Mn(III) and Mn(IV). The origins of the splittings are indicated in sans serif type at the upper left corner. The small nuclear Zeeman and quadrupole interactions are not included in the figure. Energy levels drawn closely spaced are degenerate. Mn(III) m_I values are indicated in vertical italic type to the right both above and below the levels, while Mn(IV) m_I values in each Mn(III) m_I manifold are enumerated directly to the right of the levels. EPR transitions leading to peaks 1 and 9 are indicated with the bold arrows between m_S manifolds. As discussed in the text, the EPR transition labeled 9 originates from three distinct $\{m_{I_{Mn(III)}}, m_{I_{Mn(IV)}}\}$ combinations: $\{m_{I_{Mn(III)}} = -1/2, m_{I_{Mn(IV)}} = -3/2\}$; $\{m_{I_{Mn(III)}} = +1/2, m_{I_{Mn(IV)}} = +1/2\}$; and $\{m_{I_{Mn(III)}} = +3/2, m_{I_{Mn(IV)}} = +5/2\}$. Thin arrows represent the ENDOR transitions expected to be observed at EPR peaks 1 and 9: Mn(IV) ENDOR transitions are shown as a dashed line, while Mn(III) ENDOR transitions are shown as a solid line. As discussed in the text, multiple Mn(III) and Mn(IV) ENDOR transitions originate from the degenerate states giving rise to EPR peak 9. The transitions labeled $\dagger_1$ and $\dagger_2$ and the states marked with an asterisk are discussed in the text.

These projection factors α, with values $\alpha_i = (1/2)(1 \pm \{S_1(S_1 + 1) - S_2(S_2 + 1)\}/\{S_T(S_T + 1)\})$, evaluate to 2 and -1 for high-spin Mn(III) ($S_1 = 2$) and Mn(IV) ($S_2 = 3/2$), respectively.[33] Since the intrinsic hyperfine interactions are approximately equal for Mn(III) and Mn(IV),[47,48] the effective hyperfine interactions in the coupled representation are in an approximate 2:(−1) ratio for the respective nuclei in the coupled system.[33] The small magnitude of D_i/J for both ions ensures that these complexes are in the strong exchange interaction limit and that the 2:(−1) ratio of projection factors is nearly exact.[13] Also, in the coupled representation the effective g value is quite close to those of the isolated ions ($g = 2g_{Mn(III)} - 1g_{Mn(IV)} \approx 2.0$).[13,47,48]

An isotropic energy level diagram based on eq 3 and assuming an exact 2:(−1) ratio for the effective Mn hyperfine interactions is shown in Figure 1. Each state is described by a unique set of the three quantum numbers m_S, $m_{I_{Mn(III)}}$, $m_{I_{Mn(IV)}}$, giving a total of 72 states for the $S = 1/2$, $I_{Mn(III)} = 5/2$, $I_{Mn(IV)} = 5/2$ spin system. An alternative way to visualize the states is the column plot in Figure 2 which focuses only on the $m_S = +1/2$ manifold. In this presentation of the 36 states in the $m_S = +1/2$ manifold, the height of each column in the 6 × 6 base grid corresponds to the relative energy of that $m_{I_{Mn(III)}}$, $m_{I_{Mn(IV)}}$ state. In the complementary $m_S = -1/2$ manifold (not shown) the energy surface will be inverted (i.e., the highest column above the base grid in the $m_S = +1/2$ manifold will be the furthest below in the $m_S = -1/2$ manifold).

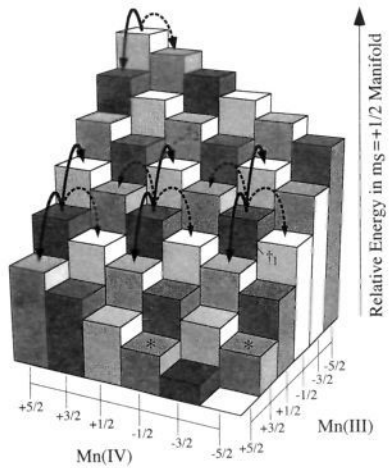

Figure 2. An alternative representation of the energy level diagram of the spin system in Figure 1 for the $m_S = +1/2$ manifold. The height of individual columns is the relative energy of that $\{m_{I_{Mn(III)}}, m_{I_{Mn(IV)}}\}$ state in the $m_S = +1/2$ manifold. Thus, columns of the same height correspond to degenerate states. The resulting 16 unique energy values give rise to 16 peaks in the EPR spectrum when connected to the mirrored energy surface representing the $m_S = -1/2$ manifold. ENDOR transitions equivalent to those in Figure 1 (in the $m_S = +1/2$ manifold) are indicated, though the multiple ENDOR transitions selected by performing ENDOR at a given field in the middle of the EPR spectrum are more clearly recognized. The clusters of arrows originating from the degenerate $\{m_{I_{Mn(III)}}, m_{I_{Mn(IV)}}\}$ columns indicate the allowed ENDOR transitions from that $\{m_{I_{Mn(III)}}, m_{I_{Mn(IV)}}\}$ combination. Solid lines are Mn(III) ENDOR transitions while dashed lines are Mn(IV) ENDOR transitions (as in Figure 1). The transitions labeled $\dagger_1$ and $\dagger_2$ are between the same two $m_{I_{Mn(III)}}$ levels. The levels marked with an asterisk exemplify the a degeneracy.

Both presentations of the isotropic energy level diagram indicate a considerable number of energy level degeneracies among the 36 states in each m_S manifold. These degeneracies occur because of the assumed 2:(−1) ratio of the effective hyperfine interactions of the two nuclei. In Figure 1, degenerate states are drawn split by a small amount for visual clarity. In Figure 2, energy level degeneracies occur for columns of equal height (and shading): for example, the degenerate $|m_{I_{Mn(III)}} = +5/2, m_{I_{Mn(IV)}} = -1/2\rangle$ and $|m_{I_{Mn(III)}} = +3/2, m_{I_{Mn(IV)}} = -5/2\rangle$ states are both marked with an asterisk in Figures 1 and 2. Allowed EPR transitions will be between states that differ only in m_S by ±1 (first-order EPR selection rules are $\Delta m_S = \pm 1$ and $\Delta m_I = 0$ for all nuclei). As an example, two EPR transitions are indicated by the bold lines between m_S manifolds in Figure 1. Though the $m_S = -1/2$ manifold is not shown in Figure 2, an EPR transition in this energy level representation would be represented by a vertical line within a column of constant $m_{I_{Mn(III)}}$ and $m_{I_{Mn(IV)}}$. Multiple degeneracies give rise to

(47) Gerritsen, H. J.; Sabisky, E. S. *Phys. Rev.* **1963**, *132*, 1507−1512.
(48) Andresen, H. G. *Phys. Lett.* **1960**, *120*, 1606−1611.

only 16 unique energy levels in each m_S manifold; hence, a 16-line EPR spectrum is observed.[33,49]

ENDOR transitions are nuclear magnetic spin transitions in which $\Delta m_I = \pm 1$ and $\Delta m_S = 0$ with only one nuclear spin projection change per ENDOR transition. When the hyperfine interaction is resolved in the EPR spectrum, the only observed ENDOR transitions are those which originate from the specific m_I value selected by the position in the EPR spectrum at which the ENDOR experiment is performed. We reported such m_I selection in the ^{55}Mn ENDOR of Mn^{2+} in SrO and $CaCO_3$ matrices.[50] Since ^{55}Mn hyperfine structure is resolved in the EPR spectrum of **1**, the ENDOR transitions are "m_I filtered" by the selection of the hyperfine peak in the EPR spectrum where the experiment is performed. However, m_I filtering in **1** is complicated by the fact that multiple m_I values are selected at EPR positions away from the high-field and low-field ends of the spectrum. The ^{55}Mn ENDOR selection rules for the Mn(III) and Mn(IV) ENDOR transitions of **1** are demonstrated in Figures 1 and 2. Figure 1 illustrates the allowed ENDOR transitions expected at the indicated EPR transitions. ENDOR transitions are indicated as dashed lines for Mn(IV) and solid lines for Mn(III). In Figure 2, allowed ENDOR transitions are from an initial $m_{I_{Mn(III)}}$, $m_{I_{Mn(IV)}}$ column to any adjacent column whose edge touches one of the edges of the initial column. Corner-to-corner transitions are not allowed since they would require a simultaneous m_I change for both ^{55}Mn nuclei. Identical ENDOR selection rules are followed in the $m_S = -1/2$ manifold (not shown). The frequency of an ENDOR transition is related to the difference in heights of the columns. Figure 2 predicts the Mn(III) ENDOR transitions to be at twice the frequency of Mn(IV) ENDOR transitions. An example of the selection rules is illustrated in Figure 2 where arrows clustered on a column show all the allowed ENDOR transitions from that column.

In addition to the hyperfine interaction, for nuclei with $I \geq 1$ the nuclear electric quadrupole term $(\vec{I}_i \cdot \mathbf{P}_i \cdot \vec{I}_i)$ in eq 3 may also be important in the ENDOR experiment. The quadrupole term arises from the interaction of the electric field gradient at the nucleus with the nuclear quadrupole moment and is observed as a first-order effect in the ENDOR spectrum. Electric field gradients arise from nonspherically symmetric charge distributions. Due to a Jahn–Teller distortion, the electronic configuration about high-spin Mn(III) (d^4) is expected to be highly nonsymmetric and should give rise to a significant nuclear quadrupole interaction. Though electronic distribution about Mn(IV) is expected to be more symmetric than for Mn(III), the cis-μ-oxo ligands to Mn(IV) may distort the electronic distribution which would lead to non-negligible quadrupolar interactions for this nucleus as well.[51] In its principal axis system, the traceless nuclear quadrupole tensor **P** can be represented by the two parameters, $P_{||} = (3/2)P_{zz} = 3e^2Qq/[4I(2I-1)] = 3e^2Qq/40$ for $I = 5/2$ and $\eta = |(P_{xx} - P_{yy})/P_{zz}|$,[52] where $P_{||}$ reflects the field gradient along the axis of the largest gradient and η is a measure of the gradient asymmetry in the plane perpendicular to that axis. Incorporating these definitions, in the principal axis system of the nuclear quadrupolar interaction the $\vec{I}_i \cdot \mathbf{P}_i \cdot \vec{I}_i$ term in eq 3 can be rewritten as

$$P_{||_i}[\{\vec{I}_{z_i}^{\,2} - (1/3)I_i(I_i+1)\} + (\eta_i/3)\{\vec{I}_{x_i}^{\,2} - \vec{I}_{y_i}^{\,2}\}] \quad (4)$$

The matrix form of the quadrupolar interaction ($\mathbf{P}_i$) in its principal axis system is

$$\mathbf{P}_i = \frac{P_{||_i}}{3}\begin{pmatrix} -(1-\eta_i) & 0 & 0 \\ 0 & -(1+\eta_i) & 0 \\ 0 & 0 & 2 \end{pmatrix} \quad (5)$$

Experimental Section

Pulsed EPR. The laboratory-built ESE–ENDOR spectrometer has been described in detail elsewhere.[50,53] All experiments were carried out at X-band (10.217 or 10.955 GHz) at a temperature of 4.2 K utilizing the Davies ENDOR pulse sequence ($\pi - T - \pi/2 - \tau - \pi - \tau -$ echo) in which an rf pulse driving nuclear spin transitions is applied during the time T.[54] ESE–EPR spectra were recorded by monitoring the amplitude of a two-pulse echo ($\pi/2 - \tau - \pi - \tau -$echo) as a function of field.

Samples. The ^{15}N-labeled $[(bipy)_2Mn(III)O_2Mn(IV)(bipy)_2](ClO_4)_3]$ was prepared as the perchlorate salt.[55] Pure crystalline sample was obtained from acetonitrile evaporation. ^{15}N-labeled 2,2′-bipyridine (lot number 2568-L) was obtained from MSD Isotopes (Division of Merck Frosst Canada, Inc., Montreal, Canada) at 99.0 atom % purity. The ^{15}N-labeled compound was utilized because deep ESE modulations in the natural abundance ^{14}N sample reduce the size of electron spin echoes.[56,57] Compound **1** was dissolved in equal aliquots of acetonitrile and dichloromethane to make a 10 mM solution. The sample was then slowly (~5–8 h) cooled to approximately 190 K and then rapidly (~1/2 h) cooled to 4.2 K. This method of sample preparation was empirically determined to give glasses suitable for performing pulsed EPR experiments.

PS II O_2-evolving membranes were prepared from fresh hydroponically-grown spinach with a slightly modified version of the "BBY" preparation[58] as described by Kim *et al.*[37] The final pellet was resuspended in buffer containing 0.4 M sucrose, 5 mM $MgCl_2$, 15 mM NaCl, 5 mM $CaCl_2$, 1 mM EDTA, 50 mM MES at pH 6.0, and 5% ethanol by volume. The PS II membranes were then loaded into a 3.8 mm o.d. quartz EPR tube and poised in the S_1 state by dark adaptation at 273 K for 15 min. Advancement to the S_2 state was obtained by 5 min illumination at a temperature of 195 K with a 120 V, 300 W Radiac IR-filtered light source.

Simulations. A computer program based on the IMSL routine EVLHF[59] was written to diagonalize a spin Hamiltonian matrix containing elements appropriate to a rhombic spin system (rhombic **g**, $\mathbf{A}_i$, $\mathbf{P}_i$, and isotropic nuclear Zeeman). ENDOR transition frequencies were calculated for each angle from the eigenvalues and bin-sorted to simulate the ENDOR spectrum. Further details of the program are provided in the following discussion and the Appendix. Simulations were performed on a VAXstation 3100 Model 76. A typical simulation time was 1 min.

Results and Discussion

^{55}Mn ENDOR of 1. The ESE–EPR spectrum of **1** is displayed in Figure 3. Sixteen ^{55}Mn hyperfine peaks are observed in the EPR spectrum. In addition, there are numerous

(49) In this paper the convention of sequentially numbering EPR peaks from low field to high field is used. In the isotropic picture, the middle eight EPR peaks arise from triple degeneracies (exactly), while EPR peaks 3, 4, 13, and 14 arise from double degeneracies (exactly), and the EPR peaks 1, 2, 15, and 16 arise from nondegenerate levels.

(50) Sturgeon, B. E.; Ball, J. A.; Randall, D. W.; Britt, R. D. *J. Phys. Chem.* **1994**, *98*, 12871–12883.

(51) Measurements of the hyperfine anisotropy of Mn(IV) and Mn(III) in **1** confirm the presence of nonspherical *unpaired* electron spin distributions about these nuclei (ref 13).

(52) Abragam, A.; Bleaney, B. *Electron Paramagnetic Resonance of Transition Ions*; Dover Publications: New York, 1986; pp 166–167.

(53) Sturgeon, B. E.; Britt, R. D. *Rev. Sci. Instrum.* **1992**, *63*, 2187–2192.

(54) Davies, E. R. *Phys. Lett.* **1974**, *47A*, 1–2.

(55) Cooper, S. R.; Calvin, M. *J. Am. Chem. Soc.* **1977**, *99*, 6623–6630.

(56) Britt, R. D. Ph.D. Thesis, Department of Physics, Lawrence Berkeley Laboratory, University of California, Berkeley, 1988.

(57) Sturgeon, B. E. Ph.D. Thesis, Department of Chemistry, University of California, Davis, 1994.

(58) Berthold, D. A.; Babcock, G. T.; Yocum, C. F. *FEBS Lett.* **1981**, *134*, 231–234.

(59) IMSL Math/Library IMSL, Inc., Houston, TX, 1990.

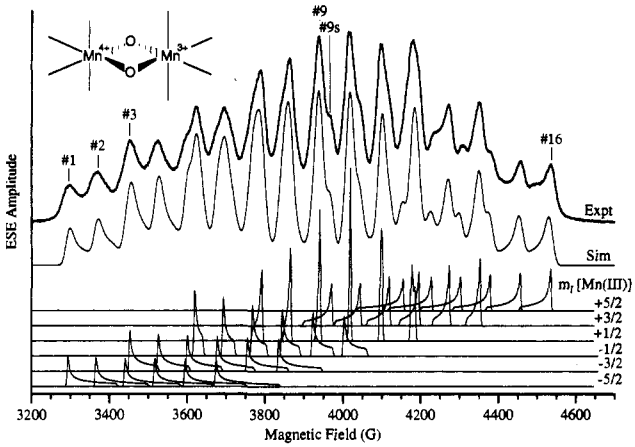

Figure 3. Experimental and simulated ESE−EPR spectra for **1**. The peaks where the ENDOR spectra presented in Figure **4** were obtained are marked. The simulated traces at the bottom of the graph show the EPR contributions for each $\{m_{I_{Mn(III)}}, m_{I_{Mn(IV)}}\}$ combination. After Gaussian smoothing, the sum of these 36 traces forms the simulated EPR spectrum marked Sim. The spectra were simulated with second-order perturbation theory expressions and use the **g** and hyperfine values given in the Table 1. Traces with the same vertical offset correspond to the labeled $m_{I_{Mn(III)}}$ value. With increasing field in each $m_{I_{Mn(III)}}$ set the $m_{I_{Mn(IV)}}$ values are +5/2, +3/2, +1/2, −1/2, −3/2, and −5/2. The Mn_2O_2 core in **1** is shown as an inset. Experimental parameters were the following: temperature, 4.2 K; ν_{MW}, 10.955 GHz; τ, 150 ns; π MW pulse, 30 ns; $\pi/2$ MW pulse, 15 ns; MW power, ≈ 40 W; ΔB, 2 G; repetition rate, 200 Hz. Each point is the average of 60 echoes.

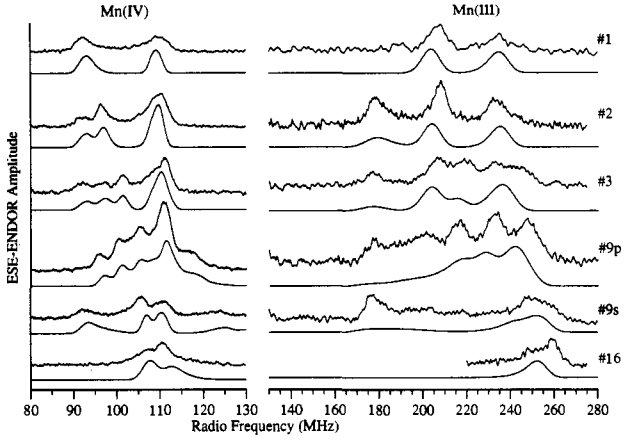

Figure 4. Experimental Davies ^{55}Mn ESE−ENDOR and simulated ESE−ENDOR spectra of **1** obtained at field positions indicated in Figure 3. The simulated spectra were obtained by diagonalization of the spin Hamiltonian as discussed in the text. Simulation parameters are summarized in Table 1. The lower frequency transitions are ascribed to Mn(IV) and the higher frequency transitions to Mn(III). The frequency axis for the Mn(IV) spectra is expanded 2-fold compared to the frequency axis of Mn(III). Experimental conditions were as follows: temperature, 4.2 K; π MW pulse, 30 ns; $\pi/2$ MW pulse, 15 ns; MW power, ~ 40 W. Each point is the average of 1000−3200 echoes. These conditions apply to all scans except Mn(III) at EPR peak 1: ν_{MW}, 10.955 GHz; τ, 150 ns (210 ns for peak 9 and shoulder 9 for Mn(III)); $\Delta\nu_{rf}$, 0.2 MHz Mn(IV), 0.5 MHz Mn(III); rf pulse, 20 μs centered in 30 μs T; rf power: ~200 W; repetition rate, 1000 Hz; magnetic fields (G), 1, 3295; 2, 3368; 3, 3452; 9 (peak), 3938; 9 (shoulder), 3966; 16, 4536. The conditions for Mn(III) at peak 1 are as follows: ν_{MW}, 10.217 GHz; τ, 350 ns; $\Delta\nu_{rf}$, 1.0 MHz; rf pulse, 36 μs centered in 40 μs T; rf power, ~100 W; repetition rate, 200 Hz; magnetic field (G), 1, 3032.

shoulders. A second-order perturbation theory simulation based on eq 3 is displayed below the experimental spectrum (*vide infra*).[60]

^{55}Mn ESE−ENDOR spectra collected at selected field positions across the EPR spectrum of **1** are presented in Figure 4. Simulated spectra are shown below each experimental trace (*vide infra*). The ENDOR spectra of both the Mn(IV) and Mn(III) (Figure 4) are centered at approximately $A/2$ for the respective ions, indicating that the large hyperfine interactions dominate the ENDOR spectra of Mn(III) and Mn(IV). Note the relative simplicity of ENDOR spectra obtained at "edge" EPR peaks (1 and 16) in contrast to the complexity of ENDOR spectra obtained in the middle of the EPR spectrum. Figures 1 and 2 illustrate why simple ENDOR spectra are observed at EPR peaks 1 and 16 for Mn(IV) and peaks 1, 2, 15, and 16 for Mn(III). For ENDOR performed at these "edge peaks", only $m_I = +5/2 \rightarrow +3/2$ or $m_I = -5/2 \rightarrow -3/2$ transitions can occur for each nucleus, giving only two ENDOR transitions (one in each of the two electron spin manifolds designated ν_- and ν_+ in order of increasing frequency). The spectral patterns observed at the ends of the EPR spectrum are utilized as starting points in simulating the ENDOR spectra for both Mn(III) and Mn(IV). Closer inspection of these edge ENDOR data for each nucleus clearly reveals the importance of the nuclear quadrupole interaction: Mn(IV) ENDOR transitions at EPR peak 1 are split by ~17 MHz, much greater than $2\nu_I$ for ^{55}Mn at this field (6.9 MHz). The ENDOR transitions at EPR peak 16 are not separately resolved; the splitting here is less than $2\nu_I$. A similar trend is observed in the data for the Mn(III) ion, though the magnitude of the splitting at low field is even larger (~25 MHz) at EPR peak 1. The fact that these trends originate from the quadrupole interactions is confirmed by our simulations (*vide infra*).

Figure 4 also shows the significantly more complex ENDOR spectra obtained in the middle of the EPR spectrum. Figure 2 helps to describe the complicated ENDOR spectrum observed at a representative central peak (peak 9), with the arrow clusters representing ENDOR transitions originating from three degenerate $m_{I_{Mn(III)}}$, $m_{I_{Mn(IV)}}$ combinations in the $m_S = +1/2$ manifold. Counting the transitions indicated by the arrows in Figure 2, a total of ten Mn(IV) (five in each m_S manifold) and eight Mn(III) (four unique transitions in each m_S manifold, two of the six arrows in Figure 2 connect states already coupled in the opposite direction[61]) ENDOR transitions are expected at this EPR peak. The same 10 Mn(IV) ENDOR transitions are expected across the middle of the EPR spectrum while different Mn(III) ENDOR transitions are expected in this portion of the EPR spectrum depending on the m_I values selected. Only six Mn(III) ENDOR transitions will be observed when $m_{I_{Mn(III)}} = \pm 5/2$.

Markedly different ENDOR spectra are observed at peaks and their adjacent shoulders in the ESE−EPR spectrum. Examples include both Mn(IV) and Mn(III) ENDOR spectra collected at peak 9 and the high-field shoulder of peak 9. Simulations suggest that these dramatic effects arise from m_I selection due to the lack of perfect alignment of the three EPR

(60) Weltner, W., Jr. *Magnetic Atoms and Molecules*; Dover: New York, 1983; pp 65−70.

(61) The ENDOR frequency of a transition where m_I increases (i.e., $m_I = -1/2 \rightarrow +1/2$ marked as $\dagger_2$ in Figures 1 and 2) is identical to the frequency for the same transition in which m_I decreases (i.e., $m_I = +1/2 \rightarrow -1/2$ marked as $\dagger_1$ in Figures 1 and 2), or in the language of Figure 2, a peak will occur in the ENDOR spectrum at the same frequency from a "jump up" or a "jump down". Figures 1 and 2 establish which m_I values will be selected when performing ENDOR on one of the middle eight peaks of the EPR spectrum: the three EPR transitions will have $m_{I_{Mn^{4+}}}$ values, skipping a value of m_I (i.e., $m_{I_{Mn^{4+}}} = +5/2, +1/2, -3/2$ or $m_{I_{Mn^{4+}}} = +3/2, -1/2, -5/2$), and three consecutive $m_{I_{Mn^{3+}}}$ values (i.e., +3/2, +1/2, −1/2, though any three consecutive m_I values are possible).

transitions which comprise this peak in the EPR spectrum. Since the ENDOR spectrum is dependent upon the EPR spectrum, it becomes important to consider a more complex picture of the EPR spectrum, including anisotropies and nonperfect degeneracies.

The presence of anisotropy in **g**, $\mathbf{A}_{Mn(III)}$, and $\mathbf{A}_{Mn(IV)}$ brings an angular dependence to the energy levels which results in broad EPR powder patterns. These interactions exhibit axial symmetry.[62] Powder pattern simulations for the 36 EPR transitions are shown in Figure 3 along with the smoothed summation which closely matches the experimental spectrum. The peaks in the simulated powder patterns originate from molecular orientations in which the angle between the magnetic field and the unique axis of the hyperfine interaction is 90°. Angles represented in the powder patterns monotonically approach 0° at the parallel turning points. It should be noted that transitions which were precisely degenerate in the isotropic case illustrated in Figures 1 and 2 are now no longer exactly degenerate except at certain angles. The experimental EPR peaks exhibit significant width due to unresolved superhyperfine interactions and possible strain in **g**, $\mathbf{A}_{Mn(III)}$, and/or $\mathbf{A}_{Mn(IV)}$. This gives rise to the experimentally observed 16-peak EPR spectrum where powder patterns that are not perfectly degenerate appear as shoulders on some of the peaks. The effects of m_I selection are very dramatic at peak 9 since one of the individual EPR transitions comprising this peak is separated from the other two EPR peaks by a relatively large amount.

ENDOR spectra depend on the hyperfine, nuclear quadrupole, and nuclear Zeeman interactions. The primary effect of **g** on the ENDOR spectrum is in providing an EPR filter for the ENDOR spectrum. For a single m_I value the ENDOR spectrum will consist of two transitions, designated ν_- and ν_+ in order of increasing frequency. The centroids, $(\nu_+ + \nu_-)/2$, of the maximum intensity of simulated ENDOR transitions in each m_S manifold depend strongly on the hyperfine parameters (particularly $A_\perp$) and to a lesser degree on the quadrupolar parameters (particularly $P_\parallel$). The splitting of an ENDOR spectrum for a given m_I value, $\nu_+ - \nu_-$, is a function of the nuclear Zeeman, hyperfine ($A_\perp$, $A_\parallel$), and quadrupolar ($P_\parallel$, η) parameters. While a larger $P_\parallel$ increases the splitting, for a given $P_\parallel$ increasing η decreases the splitting; thus, determining the quadrupolar parameters as accurately as the hyperfine parameters is difficult. The similar magnitude of contributions to the ENDOR splitting from the hyperfine, nuclear Zeeman, and nuclear quadrupole interactions necessitate the use of a matrix diagonalization approach rather than the perturbation approaches which have been utilized in nonlinear least-squares analyses of EPR spectra of mixed valence dinuclear Mn clusters.[12,13,63]

There are no nuclear−nuclear interactions included in eq 3, which greatly simplifies the diagonalization procedure. Since we are simulating nuclear transitions only, the spin Hamiltonians for the two ^{55}Mn nuclei can be diagonalized independently. Diagonalizing the resulting 12 × 12 matrix for a single ^{55}Mn nucleus coupled to an $S_T = 1/2$ effective electron spin leads to a greater than 200-fold reduction in computational time over diagonalizing the 72 × 72 matrix that would be required to include Mn−Mn nuclear couplings. Fits to the experimental Mn(III) and Mn(IV) ENDOR spectra were done on an iterative basis. Several Mn(III) and Mn(IV) parameter sets were obtained which simulated the two-transition low-field ENDOR spectra of each ion reasonably well. Simulations using these parameter sets were compared to experimental ENDOR spectra observed at other positions in the EPR spectrum. Only one set of parameters for each nucleus was observed to give a good fit to ENDOR data collected across the EPR spectrum. The parameters determined by this procedure are summarized in Table 1.

Table 1. Spin Hamiltonian Parameters Used in EPR[a] and ENDOR Simulations of $(bipy)_2Mn(III)O_2Mn(IV)(bipy)_2](ClO_4)_3$

$g_\perp$	$g_\parallel$	ion	$A_\perp$ (MHz)	$A_\parallel$ (MHz)	$P_\parallel$ (MHz)	η	ref
1.995	1.982[b]	Mn(IV)	+212	+231	+2.0	0.3	this work
1.995	1.982[c]		+212.5[c]	+231			13
		Mn(III)	−480	−360	−4.5	0.1	this work
			−490.5[c]	−378			13

[a] Due to the small magnitude of $P_\parallel/A$, quadrupolar parameters were not included in the second-order EPR simulations presented in this work. [b] The g values used herein were those of ref 13. No optimization for these parameters was performed. [c] The slightly rhombic hyperfine parameters of ref 13 were converted to axial parameters for comparison with this work according to $\perp = (x + y)/2$ and $\parallel = Z$.

The importance of hyperfine anisotropy on both EPR and ENDOR spectra is exemplified by the presence of a third "anomalous" peak in the ENDOR spectrum of Mn(III) obtained at EPR peak 2. Since EPR peak 2 (largely) arises from the same $m_{I_{Mn(III)}}$ value as EPR peak 1, a similar Mn(III) ENDOR spectrum is expected. However, along with the two Mn(III) peaks obtained at EPR peak 1, an additional peak at lower frequency (~180 MHz) is observed in the EPR peak 2 ENDOR spectrum. The large hyperfine anisotropy, particularly of Mn(III), mandates that ENDOR simulations take into account the fact that only angles selected in the EPR spectrum by the experimental choice of resonant field will contribute to the ENDOR spectrum (see the Appendix for details). The large hyperfine anisotropy of Mn(III) has the effect of distributing ENDOR intensity for a single m_I value of the Mn(III) ion over a larger frequency range than for Mn(IV); hence, angle selective effects of the EPR spectrum have a greater importance for Mn(III). Angle and m_I selected ENDOR simulations (Figure 5) reveal that ENDOR intensity for the two expected ENDOR transitions (those observed at EPR peak 1 as well as 2) arises from EPR intensity at the perpendicular turning point of EPR transition 2 (marked ⊥ in Figure 5) and that ENDOR intensity for the anomalous peak arises from the same $m_I = -5/2 \rightarrow -3/2$ transition, but from an intermediate set of angles, close to the parallel turning point of EPR transition 1 (marked ξ in Figure 5). EPR angle selection is also important in the ENDOR spectra of Mn(III) collected at other positions in the EPR envelope.

The paucity of anomalous angle-selected peaks in the Mn(IV) ENDOR spectra is a consequence of two factors. Most importantly, the smaller hyperfine anisotropy of Mn(IV) makes the ENDOR powder pattern narrower than for Mn(III) so angle effects are not distinctly resolved.[64] Secondly, for Mn(IV), the magnitude of the perpendicular component of the hyperfine interaction is smaller than that of the parallel one ($|A_\perp| < |A_\parallel|$); hence, anomalous angle-selected peaks occur at higher frequency than the more intense perpendicular peaks. This is the region of the spectrum where ENDOR transitions associated with other m_I values occur; hence, angle-selected peaks tend to be overlapped by ENDOR transitions involving other m_I values. On the other hand, $|A_\perp| > |A_\parallel|$ for Mn(III), so angle-selected peaks occur at lower frequency than the perpendicular peaks, a

(62) The quadrupolar interactions are also angularly dependent and are important in discussing ENDOR spectra. However, the relatively small magnitude of quadrupole interactions present in this system (*vide infra*) does not significantly affect the EPR spectra of **1**.

(63) Ivancich, A.; Barynin, V. V.; Zimmermann, J.-L. *Biochemistry* **1995**, *34*, 6628−6639.

(64) Mn(IV) ENDOR spectra collected across EPR peak 1 do show angle selection effects where the ENDOR frequency changes as the field (angle) is tracked across the perpendicular turning point of EPR peak 1 (data not shown).

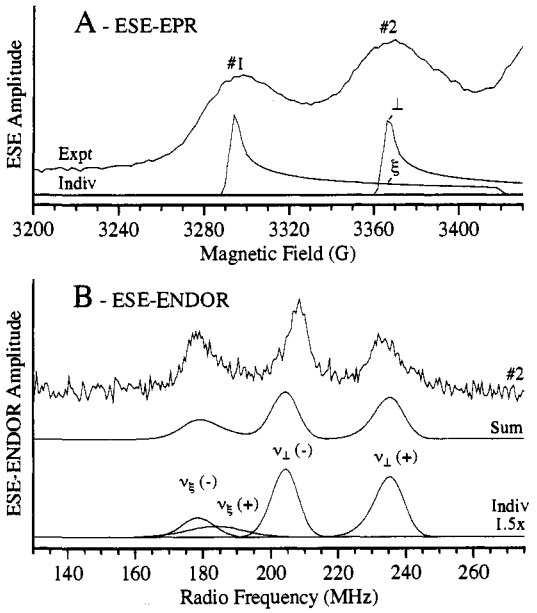

Figure 5. (A) Blowup of the ESE−EPR spectrum showing the low-field edge of the EPR spectrum. The trace labeled "Expt" is the experimental spectrum presented in Figure 3. The traces labeled "Indiv" are the contributions to the EPR spectrum from the $\{m_{I_{Mn(III)}} = -5/2, m_{I_{Mn(IV)}} = +5/2\}$ and $\{m_{I_{Mn(III)}} = -5/2, m_{I_{Mn(IV)}} = +3/2\}$ EPR powder patterns. The labeled features ($\perp$, ξ) in the EPR simulations give rise to associated ENDOR features in panel B. (B) ESE−ENDOR spectrum showing the effects of m_I and angle filtering on the ENDOR spectrum. The features marked $\nu_\perp(\pm)$ are the contributions to the ENDOR spectrum arising from the EPR perpendicular turning point of the $\{m_{I_{Mn(III)}} = -5/2, m_{I_{Mn(IV)}} = +3/2\}$ EPR transition. The features marked $\nu_\xi(\pm)$ are the contributions to the ENDOR spectrum arising from the angle packet ξ. The trace labeled #2 is the experimental ENDOR spectrum at EPR peak 2 (from Figure 4), the traces labeled "Indiv" are the individual ENDOR transitions (for each set of field-selected angles ($\perp$ and ξ) in each m_S), and the trace labeled "Sum" is the sum of the individual simulated transitions.

spectral region where no perpendicular transitions occur and little ENDOR intensity is present.

All simulated spectra (EPR and ENDOR) are derived from the set of parameters in Table 1. Due to their small magnitudes, the quadrupole terms are not included in the second-order EPR spectral simulations. Our hyperfine parameters are in reasonable agreement with those obtained from EPR simulations by Zheng *et al.*[13] A larger deviation in the value of $A_{||}$ between our results and those of Zheng *et al.* is expected on account of the relative lack of sensitivity to $A_{||}$ compared to $A_\perp$ of both EPR and ENDOR. Rhombic hyperfine interaction matrices were not necessary to obtain satisfactory simulations. Rotating the principal axes of the hyperfine and/or quadrupolar interactions with respect to the **g** axes (>15°) resulted in poorer fits to the experimental ENDOR data. The quadrupole parameters obtained on **1** represent the first determination of ^{55}Mn nuclear quadrupolar coupling constants in a mixed valence Mn cluster. The value of $P_{||}$ for Mn(IV) in **1** (+2.0 MHz) is slightly larger than observed for Mn in many monomeric high-spin Mn^{2+} systems (−1.0 to +2.5 MHz),[65] while the value of $P_{||}$ for Mn(III) in **1** is significantly larger (4.5 MHz).

The signs of the effective hyperfine parameters were *a priori* assigned to be consistent with negative intrinsic hyperfine couplings of the isolated ions and the signs of the projection factors. The fact that $P_{||}$ is of opposite sign for the two ions suggests that the electronic distribution about the nuclei is different. The sign of $P_{||}$ is dependent upon the topology of the nonspherical electron distribution, giving rise to the nuclear quadrupole interaction: oblate and prolate topologies will give opposite signs of $P_{||}$ arising from the opposite sign of the external field gradient.[66] The d_{z^2} electron of Mn(III) tends to elongate the electron cloud along a line perpendicular to the $[Mn_2O_2]^{3+}$ plane. The bond lengths in **1**, where $r^{\perp}_{Mn(III)-N} \approx 2.21$ Å, $r^{plane}_{Mn(III)-N} \approx 2.13$ Å, and $r^{plane}_{Mn(III)-O} \approx 1.85$,[67] are consistent with this interpretation.[32] Given the opposite sign of $P_{||}$ for Mn(IV) compared to $P_{||}$ for Mn(III), the electron cloud in the vicinity of Mn(IV) is slightly compressed along a line perpendicular to the $[Mn_2O_2]^{3+}$ plane. Again, the crystallographic results support this interpretation of the Mn(IV) quadrupolar parameters: $r^{\perp}_{Mn(IV)-N} \approx 2.02$ Å, $r^{plane}_{Mn(IV)-N} \approx 2.08$ Å, and $r^{plane}_{Mn(IV)-O} \approx 1.78$ Å. The smaller magnitude of $P_{||}$ for Mn(IV) compared to $P_{||}$ for Mn(III) suggests the deviation from spherical electronic symmetry is less for Mn(IV) than Mn(III). The inequivalence of r^{plane}_{Mn-O} and r^{plane}_{Mn-N} for both Mn(III) and Mn(IV) suggests that the rhombic quadrupolar parameters are due to an asymmetric electronic topology resulting from asymmetric ligation of N and O in the $[Mn_2O_2]^{3+}$ plane. Since the nuclear quadrupole is affected by *all* electrons (paired and unpaired) interacting with the Mn nucleus, these results complement the results of Zheng and Dismukes, correlating the sign of hyperfine anisotropy ($|A_{||}| - |A_\perp|$) with the unpaired spin distributions in similar multinuclear Mn clusters.[13,21,22]

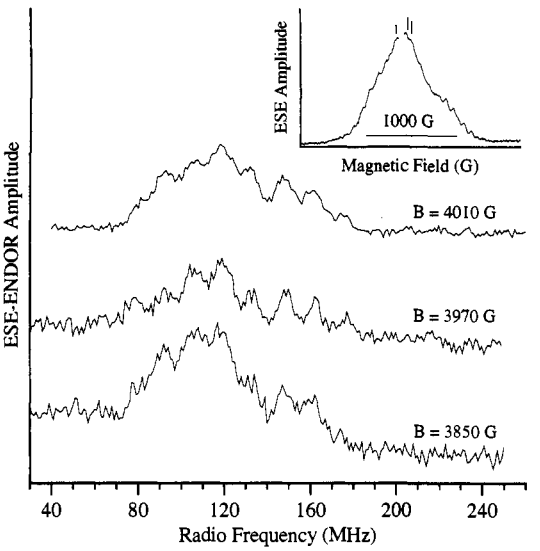

Figure 6. Davies ^{55}Mn ESE ENDOR of PS II particles trapped in the S_2 state of the Kok cycle. The inset shows the illuminated minus dark-adapted ESE−EPR spectrum (contribution from the S_2 state of the Kok cycle only) with the fields at which ENDOR was performed indicated with the vertical lines. The EPR contribution from an oxidized tyrosine radical at $g = 2$ was removed. General experimental conditions: ν_{MW}, 10.955 GHz; temperature, 4.2 K; π MW pulse, 30 ns; $\pi/2$ MW pulse, 15 ns; MW power, ~ 40 W. ESE−EPR specific conditions: τ, 240 ns; ΔB, 5 G; repetition rate, 200 Hz. Davies ESE−ENDOR specific conditions: τ, 180 ns (4010 G), 190 ns (3970, 3850 G); $\Delta\nu_{rf}$, 1.0 MHz; rf pulse, 20 μs centered in 30 μs T (4010 G), 19 μs centered in 20 μs T (3970, 3850 G); rf power: ~ 100 W; magnetic fields, 4010, 3970, 3850 G; repetition rate, 200 Hz (4010 G), 1000 Hz (3970, 3850 G).

^{55}Mn ENDOR of the S_2 State of PS II. Figure 6 displays the ^{55}Mn ESE−ENDOR obtained on the $g = 2$ multiline EPR

(65) Scharma, A. H. M. *Physica* **1973**, *68*, 279−302.

(66) Wallace, P. R. *Mathematical Analysis of Physical Problems*; Dover: New York, 1984; pp 142−144.

(67) The Mn−N distance labeled $\perp$ corresponds to the average of the Mn−N bond lengths perpendicular to the plane of the $[Mn_2O_2]^{3+}$ core, while the Mn−O and Mn−N distances labeled plane correspond to the average of either the Mn−N or Mn−O bond lengths in the plane of the $[Mn_2O_2]^{3+}$ core.

Table 2. Literature Spin Hamiltonian Parameters Used in EPR Simulations of the Native S_2 Multiline EPR Signal

		manganese hyperfine coupling (MHz)				
cluster nuclearity	g	$A(Mn_\alpha)$	$A(Mn_\beta)$	$A(Mn_\gamma)$	$A(Mn_\delta)$	ref
tetranuclear	1.987	367.2	261.6	244.8	232.5[a]	23
tetranuclear	2.020	269.0	215.8	241.0	227.0	20[b]
tetranuclear	2.0	−252.2	−252.2	−252.2	−252.2	24[c]
tetranuclear	(2.01, 1.97)	(−277, −363)	(−277, −363)	(+266, +288)	(+250, +226)	21[d]
dinuclear	(1.965, 1.966, 1.993)		(−548, −650, −172)		(+263, +367, +140)	

[a] In accordance with the effective hyperfine values suggested by our ENDOR spectra we eliminate ~60 MHz hyperfine coupling in favor of the ~230 MHz hyperfine coupling for Mn_δ. Only the magnitude of hyperfine interactions is given in ref 23. [b] Kusunoki specifies a 3Mn(IV)1Mn(III) oxidation state model with Mn_α and Mn_β in the table corresponding to an exchange-coupled Mn(III,IV) pair. [c] The work of Belinskii focuses on the effect of different coupling schemes between four Mn ions and the subsequent effects on the EPR spectrum. He does not claim these parameters are a "best fit" to the multiline spectrum. [d] Axial parameters are indicated as (⊥, ||). Zheng and Dismukes specify a 1Mn(IV)3Mn(III) oxidation state model in which Mn_γ and Mn_δ in the table correspond to an exchange-coupled Mn(III,IV) pair. [e] Rhombic parameters are indicated as (x, y, z). Åhrling and Pace specify Mn_β as Mn(III) and Mn_δ as Mn(IV). The quadrupolar parameters used in their EPR simulation are, for Mn(III), $P_{||}$ = 74.0 MHz and η = 0.14 and, for Mn(IV), $P_{||}$ = 77.9 MHz and η = 0.05.

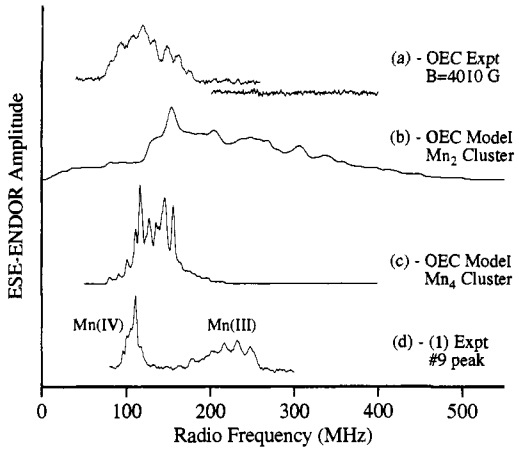

Figure 7. Experimental and simulated ENDOR spectra for the S_2 state of the OEC. Trace a is the experimental spectrum recorded at B = 4010 G (from Figure 6), and the slightly offset trace represents the high-frequency portion of the ENDOR spectrum (to 400 MHz). Trace b is a simulation using the spin Hamiltonian parameters $\mathbf{g}$, $\mathbf{A}_i$, and $\mathbf{P}_i$ for the dinuclear Mn cluster model of Åhrling and Pace[25]. Trace c is a simulation using a slightly modified set of spin Hamiltonian parameters ($\mathbf{g}$, $\mathbf{A}_i$) for tetranuclear Mn cluster model of Zheng and Dismukes[21] with quadrupole parameters fixed at $P_{||}$ = +7.0 MHz and η = 0.1 for all four Mn ions. The hyperfine parameters are as in Table 2 for ref 21, except for Mn_γ for which $A_\perp$ = +211 MHz and $A_{||}$ = +280 MHz. As a comparison, the ENDOR spectrum of **1** obtained at peak 9 is shown as trace d.

signal of the S_2 state of the OEC. The field-swept ESE−EPR spectrum is displayed in the inset. This EPR absorption spectrum consists of a broad near-Gaussian line shape with some superimposed hyperfine structure. The numerical field derivative of this EPR absorption line shape closely matches the field-modulated derivative CW EPR line shape.[35,36] The three ESE−ENDOR traces in the main portion of Figure 6 were obtained at the three field positions indicated by lines in the ESE−EPR spectrum corresponding to neighboring peaks in the CW EPR spectrum. These spectra were obtained on a PS II sample advanced to the S_2 state of the oxygen-evolving cycle[14] by 5 min of illumination at a temperature of 195 K. Several relatively well defined transitions are observed, the frequencies of which are relatively constant at the three field values examined. Figure 7 presents experimental ENDOR spectra for both the OEC in the S_2 state (a) and **1** at EPR peak 9 (d). Simulated spectra b and c will be discussed below. As emphasized in Figure 7, the frequency range over which ^{55}Mn ENDOR transitions are observed is much narrower (70−180 MHz) than observed for **1** (90−280 MHz). Parallel data recorded on dark-adapted samples poised primarily in the S_1 state show none of these ENDOR transitions.

Both dinuclear and tetranuclear Mn cluster models have been utilized in recent simulations of the g = 2 multiline EPR spectrum.[20−25] The simulations of Bonvoisin *et al.*[23] and Kusunoki[20] use four inequivalent isotropic Mn hyperfine couplings. However, appreciable hyperfine anisotropies are known to be present in the Mn(III)Mn(IV) model systems, and recent simulations by Zheng and Dismukes[21,22] use four inequivalent Mn ions with anisotropic hyperfine couplings. In contrast to these tetranuclear models, Åhrling and Pace[25] have simulated the multiline spectrum assuming a dinuclear cluster model with large rhombic hyperfine anisotropy and very large nuclear quadrupolar couplings. The various parameters used to simulate the multiline EPR spectrum of the OEC in the S_2 state are summarized in Table 2. Each of these simulations gives a reasonably good match to the CW EPR line shape even though the underlying models are very different. It is clear that EPR spectroscopy alone does not provide enough spectral information to uniquely determine the origin of the signal. This is the major motivation for introducing ^{55}Mn ENDOR to the study of the PS II Mn complex. The ENDOR spectrum depends differently on the same set of spin Hamiltonian parameters needed to determine the EPR spectrum. The quadrupolar and hyperfine parameters can be obtained more accurately with ENDOR than with EPR, while a simulation of the EPR spectrum is clearly needed to determine the g values. A valid structural model for the OEC must successfully predict both EPR and ENDOR spectra.

We first address the dinuclear Mn cluster model of Åhrling and Pace.[25] The methodology developed to analyze the ENDOR of **1** can be utilized to simulate the ^{55}Mn ENDOR spectrum that would result from the spin Hamiltonian parameters obtained from their dinuclear Mn simulation of the g = 2 multiline. The simulation for a field of 4010 G is shown in Figure 7, trace b, and can be compared to the actual experimental ENDOR data of trace a.[68] The poor match between the experimental and simulated spectra reveals that the parameters used to successfully simulate the multiline EPR signal do not adequately describe the ^{55}Mn ENDOR. Significant ENDOR intensity in the simulated spectrum occurs over a large frequency range from 50 to 400 MHz. This large spread in frequency arises from both the large rhombic hyperfine terms and the extremely large quadrupole terms required in the dinuclear Mn simulation to get a good fit to the experimental EPR spectrum. This simulated ENDOR spectrum is significantly broader than the ENDOR spectrum of the dinuclear Mn cluster in **1** because of the large

(68) No m_I or angle selection was utilized in this ENDOR simulation because of the inaccuracy of the perturbation theory EPR filter with the large quadrupolar couplings used in this simulation. However, the majority of simulated ENDOR intensity lies well above the 180 MHz maximum frequency of the experimental spectrum.

anisotropic terms. In contrast, as discussed above, the experimental spectrum of the PS II multiline is significantly narrower than that of **1**. We conclude that the extremely large magnitudes and anisotropies of hyperfine and quadrupole parameters proposed for this dinuclear EPR simulation are inconsistent with the experimental ENDOR spectrum. A better simulation of the experimental ENDOR data using the dinuclear cluster model can be obtained if the hyperfine couplings are reduced in magnitude and set nearly equivalent for the Mn(III) and Mn(IV) ions along with a significant reduction in the size of the quadrupolar interactions. However, the resulting parameters no longer give adequate simulations of the multiline EPR spectrum (not shown). We thus conclude that the experimental EPR **and** ENDOR data together cannot be adequately described by a dinuclear model. The experiments indicate that *the water-oxidizing manganese cluster of PS II does not exist as an isolated dinuclear manganese cluster.*

The experimental ENDOR spectra of the multiline EPR signal cover a relatively small frequency range, indicating that the contributing hyperfine interactions are relatively similar in magnitude. As described above, this is a very different situation than observed experimentally for **1** or predicted theoretically for the dinuclear Mn cluster model of the OEC.[69] However, the small range of effective hyperfine values observed in the ENDOR spectra of the OEC is consistent with recent simulations of the multiline EPR signal assuming a tetranuclear Mn cluster (Table 2).[70] Since it is clear from EPR and our ESE−ENDOR that appreciable hyperfine anisotropy exists in the dinuclear model complexes, we started the ENDOR simulations using the parameters from the multiline EPR signal simulation of Zheng and Dismukes[21] that includes hyperfine anisotropy for each of the four Mn ions. Figure 7c displays an ENDOR simulation utilizing hyperfine parameters that are almost identical to those utilized by Zheng and Dismukes with the addition of quadrupolar parameters $P_{||}$ of +7.0 MHz and $\eta = 0$ for each Mn ion.[71] The perpendicular component of $A(\mathrm{Mn})_\gamma$ in our ENDOR simulation is reduced by 15 MHz (from 226 to 211 MHz) with respect to the value utilized by Zheng and Dismukes (Table 2).[21] This small change, necessary to match the low-frequency edge of the experimental ENDOR spectrum, provides a negligible change in the simulated EPR spectrum (not shown). The frequency range over which appreciable ENDOR intensity occurs in the tetranuclear simulation closely matches the experimental spectrum, and the number and spacing of resolved ENDOR peaks are reasonably matched. The degeneracy of EPR transitions near the center of the EPR spectrum is high for the 1296-state tetranuclear system, and the fact that the ENDOR peaks do not shift appreciably over the modest field range over which we have obtained spectra is not surprising in this case since essentially all m_I values for each of the four ^{55}Mn nuclei will be contributing throughout this central region.[72] The simulated ENDOR features at a given field position toward the center of the EPR spectrum are relatively insensitive to small changes in the quadrupolar parameters, and a careful analysis with m_I and angle selected simulations of experimental ENDOR spectra obtained over a much wider field range will be required to accurately determine the quadrupolar parameters and to specify a unique set of hyperfine parameters for the Mn cluster. However, it is clear that unlike the dinuclear model, a tetranuclear model for the Mn cluster provides a basis for the simulation of both EPR and ^{55}Mn ENDOR spectra with the same spin Hamiltonian parameter set.

Conclusions

The EPR spectrum of the dinuclear mixed valence Mn(III)-Mn(IV) complex di-μ-oxo-tetrakis(2,2′-bipyridine)dimanganese-(III,IV) (**1**) is deleteriously affected by significant spectral overlap, with only 16 peaks resolved out of a total of 36 EPR transitions. This is an interesting system for analysis because the EPR line shape is largely determined by ^{55}Mn hyperfine interactions which are also the dominant terms in the ENDOR spectrum. The Davies ESE−ENDOR technique enables us to resolve the nuclear spin transitions for ^{55}Mn nuclei of both the Mn(III) and Mn(IV) ions. The ENDOR spectra obtained at the outermost pairs of lines in the EPR spectrum are the simplest to interpret because the ENDOR transitions originate from unique ^{55}Mn nuclear spin states. In contrast, ENDOR spectra obtained in the central region of the EPR spectrum contain multiple ^{55}Mn nuclear spin transitions due to the degeneracy of states giving rise to EPR transitions in the central region of the EPR spectrum. Superposition of multiple ENDOR transitions results in appreciable structure in the powder pattern ENDOR peaks obtained in this region. Because of hyperfine anisotropy for both ions, particularly for Mn(III), there are significant "angle selection" effects which must be included in ENDOR simulations as well as the selective inclusion of initial nuclear spin states. Angle-selected powder pattern simulations performed across the EPR spectrum give good fits to the experimental data with the following parameters: for Mn(IV), $A_\perp = +212$ MHz, $A_{||} = +231$ MHz, $P_{||} = 3e^2Qq/40 = +2.0$ MHz, and $\eta = 0.3$, and for Mn(III), $A_\perp = -480$ MHz, $A_{||} = -360$ MHz, $P_{||} = -4.5$ MHz, and $\eta = 0.1$.

^{55}Mn ENDOR data were also recorded for the $g = 2$ multiline EPR signal arising from Mn in the S_2 state of the PS II oxygen-evolving complex. A recent simulation has invoked a dinuclear Mn cluster origin for this signal, with the deviations between the multiline EPR signal and those of dinuclear Mn model compounds such as **1** attributed to exceedingly large nuclear quadrupolar couplings as well as larger hyperfine anisotropy for the two ^{55}Mn nuclei.[25] In the analysis of the Mn(III)-Mn(IV) model compound we developed general methods for analyzing the ^{55}Mn ENDOR of dinuclear Mn complexes. Assuming a dinuclear Mn cluster, spin Hamiltonian parameters

(69) The EPR line shape of a dinuclear Mn(II)Mn(III) model complex exhibits a rhombic **g** that vaguely resembles that of the OEC in the S_2 state. Diril, H.; Chang, H.-R.; Nilges, M. J.; Zhang, X.; Potenza, J. A.; Schugar, H. J.; Isied, S. S.; Hendrickson, D. N. *J. Am. Chem. Soc.* **1989**, *111*, 5102−5114. This is not a likely candidate for the S_2 state EPR signal since the hyperfine interactions are quite different for the Mn(II) and Mn(III) ions and would yield an ENDOR spectrum analgous to that of **1** since the projection factors are 7/3 and −4/3 and the contributions of the individual Mn ions should be resolved. Additionally, X-ray absorption edge studies of the OEC in the S_2 state strongly argue against the presence of a divalent Mn ion in the S_2 state. Yachandra, V. K.; Derose, V. J.; Latimer, M. J.; Mukerji, I.; Sauer, K.; Klein, M. P. *Science* **1993**, *260*, 675−679 and references therein.

(70) A ^{55}Mn hyperfine coupling in PS II on the order of ~60 MHz as determined by Bonvoisin *et al.*[23] is not observed in the ENDOR spectra of the OEC, though they indicate an acceptable fit is obtained when the isotropic ~60 MHz hyperfine coupling is replaced by one of ~232 MHz.

(71) In the case of a dinuclear system there is a unique mapping between the coupled and uncoupled spin system representations which makes the assignments of Mn(III) and Mn(IV) ions in the uncoupled representation straightforward based on the assignment of spin Hamiltonian parameters in the $S = 1/2$ coupled representation. This unique mapping does not exist in a tetranuclear system, where there are six independent exchange couplings. EPR simulations such as those of Zheng and Dismukes[21] that discuss explicit oxidation states typically make use of a symmetrized exchange Hamiltonian in order to link the coupled and uncoupled representations in a straightforward manner. de Paula, J. C.; Brudwig, G. W. *J. Am. Chem. Soc.* **1985**, *107*, 2643−2648. de Paula, J. C.; Beck, W. F.; Brudwig, G. W. *J. Am. Chem. Soc.* **1986**, *108*, 4002−4009. Bittl, R. *Chem. Phys. Lett.* **1993**, *215*, 279−284. See also refs 19−**24**. At this point in the ENDOR analysis we chose to discuss data supporting a tetranuclear cluster in only the coupled representation, and therefore we make no assignments as to oxidation states of individual Mn ions.

(72) No m_I or angle selection filtering is used in the simulation of Figure 7c: full powder patterns for all nuclear states are included.

which successfully simulate the EPR spectrum dramatically fail to simulate the ^{55}Mn ENDOR spectrum of the multiline EPR signal. The constraints of simulating both the EPR and ENDOR spectra rule out a dinuclear Mn origin for the multiline signal. In contrast, tetranuclear model spin Hamiltonian parameters provide good simulations of both the EPR spectrum and the ^{55}Mn ENDOR spectrum. The experimental ENDOR patterns indicate the hyperfine couplings to each of the four Mn nuclei are of comparable magnitudes. However, obtaining a unique set of spin Hamiltonian parameters for all four nuclei is not yet possible with the limited ENDOR data recorded to date for the biological cluster.

Acknowledgment. R.D.B. acknowledges a grant from the National Institutes of Health (BMT 1 R29 GM48242-01) and a NRICGP grant from the U.S. Department of Agriculture (92-01413). M.P.K. acknowledges support from the National Science Foundation (Grant DMB91-04194) and from the Director, Division of Energy Biosciences, Office of Basic Energy Sciences, U.S. Department of Energy, under Contract DE-AC-76SF00098. W.H.A. acknowledges support from the National Institutes of Health (Grant GM 38275).

Appendix

Computer Program Description. The matrix is diagonalized in a "molecule-fixed" axis system, with the defining axes being those of the **g** tensor. Full, independent rotation of the hyperfine and quadrupole interaction matrices with respect to the **g** axes is accommodated by three Euler angles for each interaction.[73] In this molecule-fixed axis system, the orientation of the external magnetic field must be rotated to generate powder patterns. The fact that full rotation of the hyperfine and quadrupole interaction matrices with respect to the **g** axes is allowed requires rotation of the lab field through the entire sphere. Both polar (θ) and azimuthal (ϕ) angles are sampled throughout the sphere by an angle-incrementing procedure outlined by Hagen *et al.*[74] By judiciously selecting starting angles and angle increment values and choosing an odd number of angles, this angle rotation scheme ensures that angles sampled in each octant of the sphere do not resample angles equivalent to those in other octants for high-symmetry cases. This is achieved by sampling slightly different angles in each octant of the sphere. No angular dependence for the transition moment is included. We have observed that there is much less than a 1% difference in the relative intensities of spectra calculated when using an angularly-dependent transition moment and when using a non-angularly-dependent transition moment. Hence, to avoid the added computational time required to calculate eigenvectors from which angularly-dependent transition moments are calculated, non-angularly-dependent transition moments are used. To diagonalize Hermitian matrices, the IMSL routine EVLHF[59] uses unitary similarity transformations to generate a real symmetric tridiagonal matrix followed by an implementation of the QL algorithm.[75]

In the simulations, angle selection is accomplished by taking the absolute value of the difference (Δ) between the second-order perturbation theory resonant EPR transition frequency for a particular $m_{I_{Mn(III)}}$, $m_{I_{Mn(IV)}}$ combination and the experimental microwave frequency. Second-order perturbation theory has been successfully used to simulate the EPR spectra for this system.[13] The ENDOR intensity is weighted by a Gaussian coefficient, $\exp[-2(\Delta/b)^2]$, where b signifies the EPR bandwidth selected by the microwave pulse. This bandwidth crudely accounts for the width of the EPR peaks. To avoid the time-consuming procedure of diagonalizing a matrix where the EPR intensity is negligible, only those EPR transitions where $\Delta \leq (3/2)b$ were diagonalized. This corresponds to 3 times the standard deviation of a Gaussian distribution.

JA9526776

(73) Zare, R. N. *Angular Momentum*; John Wiley and Sons: New York, 1988; pp 77−81.

(74) Hagen, W.; Hearshen, D. O.; Harding, L. J.; Dunham, W. R. *J. Magn. Reson.* **1985**, *61*, 233−244.

(75) Press, W. H.; Flannery, B. P.; Teukolsky, S. A.; Vetterling, W. T. *Numerical Recipies*; Cambridge University Press: New York, 1986; pp 357−363.